



Synthesis of Y-doped CeO₂/PCN nanocomposited photocatalyst with promoted photoredox performance

Hui Yang^a, Bin Xu^{a,*}, Saisai Yuan^a, Qitao Zhang^{b,*}, Ming Zhang^a, Teruhisa Ohno^{c,*}

^a School of Chemistry and Chemical Engineering, Yangzhou University, Yangzhou, 225002, China

^b International Collaborative Laboratory of 2D Materials for Optoelectronics Science and Technology of Ministry of Education, College of Optoelectronic Engineering, Shenzhen University, Shenzhen, 518060, China

^c Department of Applied Chemistry, Faculty of Engineering, Kyushu Institute of Technology, Kitakyushu, 804-8550, Japan



ARTICLE INFO

Keywords:

Doped ceria
Heterojunction
Photoredox catalysis
Synergistic effect

ABSTRACT

In this study, yttrium-doped CeO₂ was introduced into polymeric carbon nitride (PCN) through one-step hydrothermal reaction to form the Y-doped CeO₂/PCN (YCC) nanocomposited photocatalysts. Morphology of products was observed by emission scanning electron microscopy (SEM) and high-resolution transmission electron microscopy (HR-TEM). The structure of the products was characterized by X-ray diffractometer (XRD), FT-IR and Raman analysis. Optical absorption and band energy properties were investigated by UV-vis, PL and VB-XPS spectra. The X-ray photoelectron spectroscopy (XPS) results further revealed that the surface active oxygen and Ce³⁺ concentration of nanocomposited photocatalyst were significantly increased compared with pure CeO₂ and PCN counterparts. The YCC composites exhibited excellent photoredox performance under visible light irradiation, affording to 5.73- and 3.74-fold higher for RhB degradation and proton photoreduction to produce H₂ than that of pure CeO₂. The Y-doped nanocomposited means adopted in this study not only improve the optical utilization of visible light, but also effectively inhibit the recombination of photogenerated charge carriers, which are conducive to promote the photoredox performance synergistically.

1. Introduction

Recently, researchers are enthusiastically working on the development of photocatalytic materials that respond to visible light and have a narrow band gap [1–3]. Some paradigmatic metal oxide semiconductor materials just show a feeble visible light response. Thus, they merely exert better photocatalytic activity in the decomposition of water and organic pollutants field under UV irradiation. Among them, cerium oxide (CeO₂) is one of the most important rare earth metal oxides. It has been extensively used in various applications including UV blockers, polishing materials, catalysts, electrolytes, sensors, and solar cells. It is mostly due to many excellent characteristics such as low toxicity, high thermal and chemical stability, as well as its resistance to photocorrosion [4–7]. The prominence of CeO₂ material is mainly due to its large deviation in the stoichiometry as a result of easy reducibility of Ce⁴⁺ ions to Ce³⁺ ions that lead to the formation of abundant oxygen vacancies (O_v) [8,9]. It was also shown that more Ce³⁺ ions mean higher concentration of oxygen vacancies as well as better visible light absorption, which are much more facilely to generate superoxide radicals in photocatalytic dye degradation [10,11]. Therefore, oxygen defects

generated in the synthesis process play a role in promoting or inhibiting the photocatalytic performance [12,13].

The polymeric carbon nitride (denoted as PCN) is yellow powder semiconductor and it is the most stable phase at room temperature among seven phases of C₃N₄ allotropes [14]. As a fascinating metal-free polymer photo (electro)-catalyst, PCN shows many outstanding advantages, such as environmental friendliness, low fabricating cost, well physical-chemistry stability, excellent optical and electronic features. However, PCN still confronts several challenge issues, such as fast recombination rate of photoinduced electron-hole pairs, low specific surface area and limited active sites. In order to surmount these restrictions, many strategies have been developed to improve photocatalytic performance of PCN, including the development of various PCN nanostructures, doping with metal or non-metal, and constructing PCN-based heterojunction composites [15–17]. Although the quantum efficiency of PCN materials is still low so far, it provides a new, meaningful exploration to satisfy the strategy of sustainable development. Due to PCN has a moderate visible-light absorption capacity, it is often adopted as a suitable platform to complex with inorganic nanoparticles to enhance their visible-light response [18,19]. Instead of

* Corresponding authors.

E-mail addresses: twt@yzu.edu.cn (B. Xu), qitao-zhang@szu.edu.cn (Q. Zhang), tohno@che.kyutech.ac.jp (T. Ohno).

simple physical mixing between PCN and inorganic material, it is crucial to strengthen the interfacial contact between them so as to form an efficient heterojunction for involved catalytic reactions.

Therefore, we developed a novel Y-doped CeO_2 /PCN (YCC) heterojunction photocatalyst through a facile in-situ growing process of $\text{Ce}(\text{NO}_3)_3 \cdot 6\text{H}_2\text{O}$, and $\text{Y}(\text{NO}_3)_3 \cdot 6\text{H}_2\text{O}$ on PCN surface in this paper. Y-doping is a cost-effective way to hoist the concentration of oxygen vacancies and visible light absorption of CeO_2 . As far as we can concern, YCC nanocomposited heterojunction photocatalyst was fabricated herein for the first time, which obviously distinguished from most of the previous reports based on pure CeO_2 photocatalyst. The photocatalysis properties of YCC were systematically assessed by decomposition of RhB and hydrogen production under visible light illumination. Y-doped CeO_2 and PCN complement each other, which is benefitting from their highly matched band structures. In detail, the electrons generated by PCN photo-excitation transferred smoothly to the conduction band of Y-doped CeO_2 , while the photo-induced holes on valence band of the Y-doped CeO_2 flowed to valence band of PCN component. Thus the electron and hole pairs are separated effectively and the recombination rate is also decreased dramatically. In conclusion, attributing to the matchable band structures and close interfacial osculation between two components, the as-prepared YCC nanohybridized photocatalyst achieve distinctly ameliorative photoredox performance than that of single component counterpart.

2. Experimental section

2.1. Materials

Melamine, sodium phosphate, cerium nitrate hexahydrate ($\text{Ce}(\text{NO}_3)_3 \cdot 6\text{H}_2\text{O}$) and yttrium nitrate hexahydrate ($\text{Y}(\text{NO}_3)_3 \cdot 6\text{H}_2\text{O}$). All the chemical reagents used in the experiment were of analytical grade, commercially available with 99.9% purity and were used without further purification. Deionized water was used throughout the experiment.

2.2. Methods

2.2.1. Preparation of PCN

Sample PCN was prepared according to the previously reported method with a slight modification [18]. First, 15.0 g melamine was transferred to a quartz crucible and calcined at 550 °C for 4 h at a rate of 5 °C/min under air condition. After cooling to room temperature, the product was collected.

2.2.2. Preparation of Y-doped CeO_2

The typical synthetic procedures were depicted as follows and the optimal synthesis condition had been discussed previously [20]. First, 1.74 g $\text{Ce}(\text{NO}_3)_3 \cdot 6\text{H}_2\text{O}$ and 0.16 g $\text{Y}(\text{NO}_3)_3 \cdot 6\text{H}_2\text{O}$ precursors were simultaneously dissolved in 150 ml deionized water with vigorously magnetic stirring at room temperature for 30 min. Then 0.015 g Na_3PO_4 was added to the solution and stirred for 30 min. continuously. The solution was then transferred to a 200 ml Teflon-lined stainless steel autoclave and heated at 200 °C for 24 h. After cooling to room temperature, the pale yellow products were collected by centrifugation, washed with deionized water and ethanol for at least 3 times respectively, then dried at 70 °C for 18 h to collect the product of Y-doped CeO_2 .

2.2.3. Preparation of YCC

Typically, YCC heterojunction photocatalyst was prepared under the same conditions with preparation of Y-doped CeO_2 except for changing the dissolution process. Additional 0.2 g of as-prepared PCN was simultaneously dissolved in deionized water together with $\text{Ce}(\text{NO}_3)_3 \cdot 6\text{H}_2\text{O}$ and 0.16 g $\text{Y}(\text{NO}_3)_3 \cdot 6\text{H}_2\text{O}$ precursors. Other steps are the same and finally get the product of YCC.

2.3. Characterization

X-ray diffraction (XRD) was performed on a Bruker-AXS X-ray focus using Cu K α radiation source (40 kV/4 mA). The Fourier transform infrared spectroscopy (FT-IR) of the samples were recorded on KBr pressed pellets in the frequency range of 4000–400 cm^{-1} . Raman spectra were determined by In Via Laser Confocal Raman Spectrometer. Morphology and elemental mapping of the products were observed by an FE-SEM (Hitachi, S-4800) and HR-TEM (FEI, Tecnai G² F30S-TWIN, 300 KV). UV-vis diffuse reflectance spectra (DRS) were measured by a Varian Cary 5000 UV-vis spectrophotometer. The X-ray photoelectron spectroscopy (XPS) experiment was carried on a Shimadzu KRATOS AXIS-NOVA system at room temperature under 10^{-9} Pa using Al K α radiation and C 1s peak (284.6 eV) reference. The photoluminescence (PL) spectroscopy measurements were performed at an excitation wavelength of 325 nm on a fluoro-spectrophotometer (Hitachi FL4600) at room temperature. Electron paramagnetic resonance (EPR) radical signal was recorded by a Brucker EPR A200 spectrometer.

2.4. Photocatalytic activities evaluation

2.4.1. Degradation of RhB experiment

RhB was employed as a model pollutant to evaluate the photo-oxidation activity of as-prepared samples. In a typical experiment, 120 mg photocatalyst was added in 120 mL of 20 mg L^{-1} RhB aqueous solution. Prior to irradiation, the suspension was stirred in the dark for 30 min. to reach adsorption-desorption equilibrium. During the photocatalytic tests, 4 mL of the sample was taken at a given time interval, and filtered to remove photocatalyst particles. Finally, the degradation results were monitored by UV-vis spectrophotometer according to the peak value of maximum absorption ($\lambda_{\text{max}} = 554 \text{ nm}$ for RhB).

2.4.2. Hydrogen evolution experiment

Photocatalytic hydrogen evolution reactions (HER) were carried out in a bottom-irradiation vessel connected to a glass gas circulation system. 20 mg of the photocatalyst powder was dispersed in 50 mL aqueous solution containing 10 vol% triethanolamine as sacrificial agent. The deposition of 3 wt% Pt as a reducing co-catalyst was achieved by dissolving H_2PtCl_6 in the above 50 mL reaction solution and then in-situ photo-deposited for one hour. The reaction temperature was kept around 15 °C with condensation water circulation system. The amount of H_2 generated was determined using online gas chromatograph (FULI GC9790 Plus). Before detecting the photocatalytic performance, the system was fully degassed and injected Ar as carrier gases. The light source was a 300 W Xe lamp (Beijing Perfect Light Co. Ltd, PLS-SXE300) with 420 nm filter cutoff.

2.4.3. Photoelectrochemical measurements

The typical working electrode was prepared as follows: 30 mg of sample was dispersed in 30 mL of acetone and underwent 60 min ultrasonic treatment. Then 20 mg single iodine was added to enhance its ionic strength and sonicated for 30 min. Next, the product was electroplated onto a 6 cm × 1 cm conductive glass (ITO) using an electrophoresis method with a 15 V DC power supplying for 5 min. At last, the ITO glass was dried at 60 °C for 10 h to obtain the film electrode. The working electrode was irradiated by a Xe arc lamp with a 420 nm filter cutoff. Na_2SO_4 (0.1 M) aqueous solution was used as the electrolyte. Photoelectrochemical measurements were performed on an electrochemical analyzer (CHI660D, Shanghai, Chenhua) in a standard three-electrode configuration with a Pt as the counter electrode and Ag/AgCl as a reference electrode.

2.4.4. Active species trapping experiments

In order to detect active species in the photocatalytic process, $\text{K}_2\text{Cr}_2\text{O}_7$ was used as electron (e⁻) scavenger, ethylenediaminetetraacetic acid disodium (EDTA) was selected as the hole (h⁺)

scavenger, tert-butanol (TBA) was employed as the hydroxyl radical ($\cdot\text{OH}$) scavenger and 1,4-benzoquinone (BQ) was chosen as the superoxide radical ($\cdot\text{O}_2^-$) scavenger. The photocatalyst with different scavenger (1 mM) was dispersed in RhB solution (120 ml, 20 mg L⁻¹). The following processes were similar to the RhB photodegradation experiment as-described in experimental section of 2.4.1.

2.4.5. Photocatalytic reduction of Cr(VI)

The photocatalytic evaluation test of Cr(VI) was done in the GHX-2 photocatalytic reactor. Simulated visible light source system under the condition of one Xe lamp with a power of 250 W, two $\lambda > 420$ nm filters and temperature controlling in 25 °C. The photocatalytic reduction Cr(VI) efficiency test method as following: First, 120 mL 20 mg/L K₂Cr₂O₇ solution, 120 mg photocatalysts and 1 mL 100 mg/mL of formic acid were added to the reaction flask. Then setting the experimental temperature, open the circulating water, and continue stirring for 60 min in the dark to achieve the adsorption-desorption equilibrium of the photocatalyst and Cr(VI) aqueous solution. After 60 min, the Xe lamp was turned on, and 4.0 mL of the suspension reaction liquid was withdrawn from the reaction flask at regular intervals, and the K₂Cr₂O₇ solution was separated from the photocatalyst by filtration with double layers of cellulose acetate membrane (pore size is 0.22 μm). Finally, the Cr(VI) concentration in the filtrate was determined by diphenylcarbazide (DPC) spectrophotometry (the maximum absorption wavelength of the purple complex formed by DPC and Cr(VI) was $\lambda_{\text{max}} = 540$ nm).

3. Results and discussion

3.1. Morphology characterization

The morphology of YCC was characterized by SEM, TEM and HR-TEM. Figs. 1a and S1a show that CeO₂ fabricated by hydrothermal treatment exhibits an octahedral morphology with average particles size about 100 nm. As given in Figs. 1b and S1b, the as-prepared nanocrystals Y-doped CeO₂ still remain morphology of octahedra. The multi-layered block structure of PCN with smooth surface can be clearly observed from Figs. 1c and S1c. As given in Figs. 1 (d, e) and S1 (d, e) numerous CeO₂ and Y-doped CeO₂ polyhedral nanoparticles were successfully deposited on PCN resulting in the formation of the heterojunction in CeO₂/PCN and YCC, respectively. This kind of morphology has the higher specific surface area of 23.11 m²/g and 39.26 m²/g than

that of PCN and CeO₂ counterparts, which is benefit for catalytic reaction. (shown in Fig. S7) Obviously, CeO₂ nanocrystals anchored on the surface of PCN in YCC are distributed randomly, which is attributed to the indetermination distribution of amino groups within CN conjugated frameworks. As can be seen from Fig. 1f, the lattice spacing values of CeO₂ are 0.270 nm and 0.325 nm, indicating that these crystal faces are assigned to the (200) and (111) exposed crystal planes of the cubic fluorite structure of CeO₂. There are obvious interfacial transition zones between CeO₂ and PCN in YCC. Based on the above observation, we can draw the conclusion that the heterojunction of YCC is formed between the (111) and (200) planes of CeO₂ and the amorphous PCN. Besides, the energy dispersive spectrometer (EDS) measurement (Fig. S2) shows that YCC nanocomposites are composed of Y, Ce, O, C and N elements. EDS mapping results are presented in Fig. 2, it further manifests that these elements have a good distribution in the surface and bulk of the YCC. In view of the above results, it can be inferred that the YCC nano-hybridized photocatalyst was successful prepared by this facile in-situ hydrothermal treatment.

3.2. Structure characterization

Fig. 3 shows the XRD patterns of PCN, CeO₂, Y-doped CeO₂, CeO₂/PCN and YCC. As presented in Fig. 3a, two distinct peaks located at 13.1° and 27.5° are both found in pure PCN and YCC. The strongest peak at 27.5° is a characteristic peak indexed to the (002) interlayer stacking of aromatic systems for graphitic materials. The dense structure can lead to the localization of the electrons and stronger interaction between the layers [21]. The smaller angle peak at 13.08° of YCC is assigned to (100) ($d = 0.676$ nm), which is associated within-planar repeated nitride pores. The distance is slightly smaller than the size of one tris-s-triazine unit (ca. 0.730 nm), which is attributed to the presence of slightly rotational angularity in the structure.

The characteristic diffraction peaks of CeO₂ appear at 28.5°, 33.1°, 47.6° and 56.4°, corresponding to the crystal planes of (111), (200), (220) and (311) planes respectively [22,23]. The relative intensity ratios of these characteristic peaks keep consistent with the standard data reported in JCPDS card (No. 34-0394), which reveals that there is no orientation crystal growth of the as-prepared CeO₂ nanocrystals. Meanwhile, all of the diffraction lines can be indexed to the phase of CeO₂ with a cubic fluorite structure (Space group: Fm-3 m (225)). The sharp diffraction peaks of all CeO₂-contained samples suggest a high

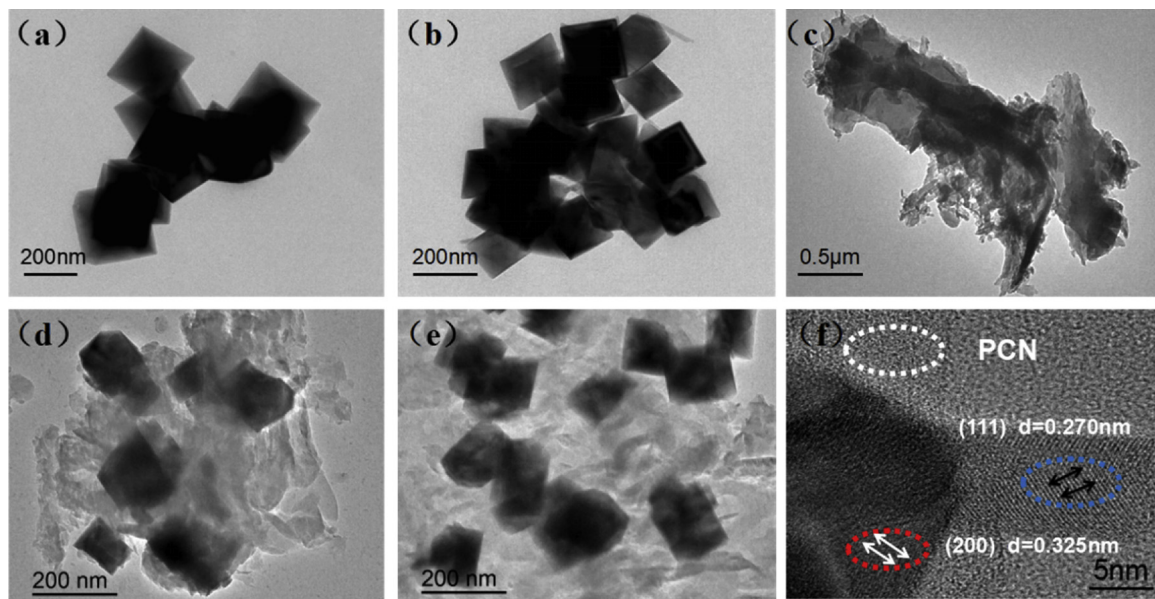


Fig. 1. TEM and HR-TEM images of (a) CeO₂; (b) PCN; (c) Y-doped CeO₂; (d) CeO₂/PCN and (e) YCC; (f) CeO₂ lattice fringe in YCC of (200) plane and (111) plane.

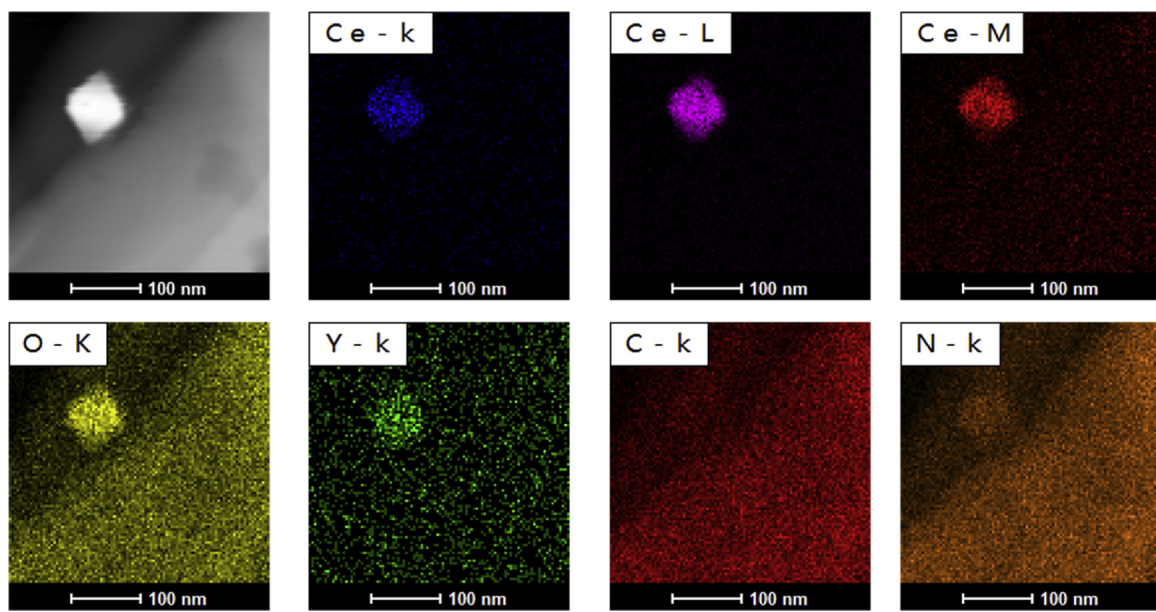


Fig. 2. EDS elemental mapping of Ce-K, Ce-L, Ce-M; O-K; Y-K; C-K and N-K.

degree of crystallinity without impurity peaks, indicating that the concentration of the Y dopant has negligible effect on crystalline phase purity of the products. However, comparing the highest XRD peak of CeO_2 with Y-doped CeO_2 (enlarged image in Fig. S3a), it makes clearly that after yttrium doping the (111) peak of CeO_2 significantly shifted from 28.58° to a lower angle of 28.43° . It indicates that crystal lattice of

Y-doped CeO_2 was expanded conspicuously due to the introduction of yttrium into the crystal structure. In general, the characteristic diffraction peaks of PCN and CeO_2 still remain in YCC.

Besides, in order to study the actual doping quantity and the doping position, Rietveld refinements were further performed on different parameters according to its diffraction lines in (given in Fig. S4) [24].

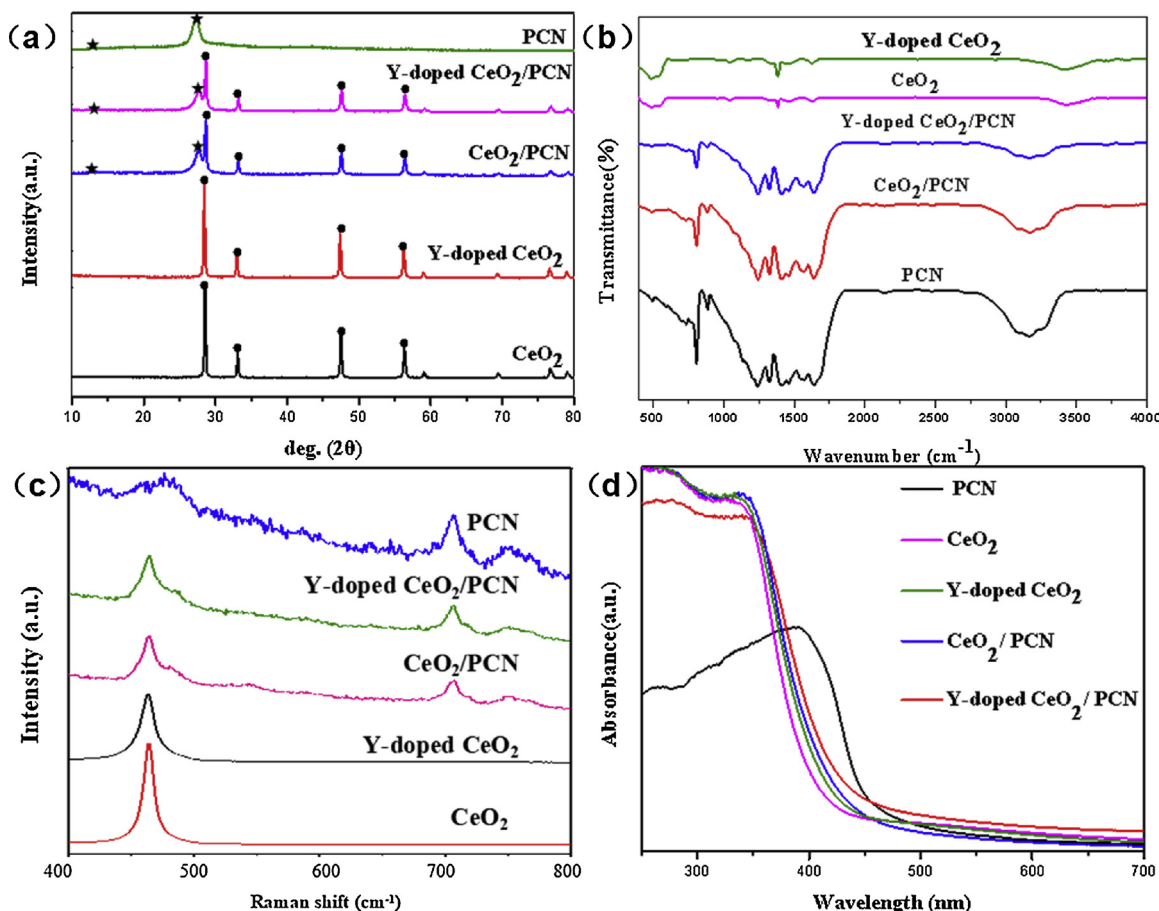


Fig. 3. Structure characterization of as-prepared samples: (a) XRD patterns; (b) FT-IR spectra (c) Raman spectra; and (d) UV-vis diffuse-reflectance spectra.

The lattice parameter value (a) of CeO_2 was changed from 5.4129 Å to 5.4325 Å (Tab.S1) after yttrium doping. The enlarged lattice parameter means that yttrium is successfully doped into the CeO_2 lattice, affording to the prominent expansion of crystal lattice. However, the lattice parameter value (a) of YCC is 5.4286 Å. This value is slightly lower than that of Y-doped CeO_2 sample. It may be due to the steric hindrance effect produced by the combination of PCN and Y-doped CeO_2 , which partly limits the entry of Y^{3+} into CeO_2 lattice. Using the Scherrer's formula, the particle size (D) of the samples was calculated (Tab.S1). The D values of Y-doped CeO_2 (45.2 nm) and YCC (58.2 nm) are slightly smaller than CeO_2 counterpart (67.3 nm) after doping by yttrium. The results are in good consistent with the SEM and TEM observations. The effect of doping weakens the changing of particle size, which derived from the crystal lattice expanding or contracting [25,26].

The FT-IR spectra of PCN, CeO_2 , Y-doped CeO_2 , CeO_2/PCN and YCC were shown in Fig. 3b. For pure PCN, the peak located at 1646 cm^{-1} is attributed to the C=N stretching vibration, while the peaks of 1565 cm^{-1} , 1408 cm^{-1} , 1320 cm^{-1} and 1238 cm^{-1} are related to stretching vibration of aromatic C–N [24]. The peak near 805 cm^{-1} is attributed to the out-of plane breathing vibration of triazine unit connection [27,28]. For pure CeO_2 , the absorption peak at 485 cm^{-1} is due to Ce–O stretching vibration [29]. In the case of YCC, the characteristic vibrations peaks of PCN and CeO_2 are both remained [30]. However, the vibration band of triazine unites at 805 cm^{-1} in YCC shifts to high wavenumber (Fig. S3b), which manifests the formation of chemical bonding between PCN and CeO_2 instead of a simple physical contact. Raman spectra of samples are also shown in Fig. 3c. A strong Raman shift at 460 cm^{-1} of CeO_2 can be assigned to F_{2g} vibration of the fluorite-type structure. When CeO_2 was doped by yttrium, F_{2g} peak shifted from 464.11 to 463.52 cm^{-1} , adequately verifying the introduction of Y ions into MO_8 in CeO_2 lattice (enlarged image in Fig. S3c). In addition, the characteristic peak of PCN appears in 476 cm^{-1} , 706 cm^{-1} and 752 cm^{-1} and they were obviously shifted in YCC, further illustrating the strong interaction between Y-doped CeO_2 and PCN [31].

For semiconductors, the absorption edge of the band follows the Eq. (1):

$$(\alpha h\nu)^n = B(h\nu - E_g) \quad (1)$$

Where α is the absorption coefficient, B is the material-depent constant, $h\nu$ is the discrete photon energy, E_g is the absorption bandgap, and n is the number of different types of electronic transitions. Calculated by Tauc plot in Fig. S3d, The band gaps of CeO_2 , Y-doped CeO_2 and PCN are 2.88 eV, 2.79 eV and 2.62 eV, respectively. The comprehensive band gaps of CeO_2/PCN and YCC are 2.72 eV and 2.66 eV, respectively. Obviously, compare with single-component CeO_2 , composite materials expressed distinct red-shift (Fig. 3d). The appropriate match of the band structure between the two components in YCC can effectively promote the separation of the photogenerated charges and accelerate the photocatalytic redox reactions.

The surface chemical states of YCC and the interaction between PCN and CeO_2 were investigated by XPS analysis. The survey spectra of YCC showed in Fig. S5 indicated that the prepared composite consists of Ce, O, Y, C and N elements, which is well consistent to EDS result.

Fig. 4a displayed Ce 3d electron core level and two group peaks were obtained (denoted as v and u) after deconvolution treatment [32,33]. According to previous studies, the labels of (U, V), (U_2 , V_2) and (U_3 , V_3) can be classified as Ce 3d_{5/2} and Ce 3d_{3/2} related to Ce⁴⁺, originating from the final state of Ce (3d⁹4f⁰) O (2p⁶), Ce (3d⁹4f¹) O (2p⁵) and Ce (3d⁹4f²) O (2p⁴), respectively. Two pairs of doublets (U_0 , V_0) and (U_1 , V_1) for the Ce 3d bond energy peak ascribed to Ce³⁺ and the double lines correspond to Ce (3d⁹4f¹) O (2p⁶) and Ce (3d⁹4f¹) O (2p⁵), respectively. Compared with CeO_2 counterpart, the peak positions of Ce³⁺/Ce⁴⁺ in YCC shifted to higher binding energy, attesting the formation of heterojunction between PCN and CeO_2 , which is in line with the literature values [32]. The relative amount of cerium in the

tervalent oxidation state was calculated by Eq. (2):

$$[\text{Ce}^{3+}] = \frac{A_{v_0} + A_{v_1} + A_{u_0} + A_{u_1}}{A_{v_0} + A_v + A_{v_1} + A_{v_2} + A_{v_3} + A_{u_0} + A_u + A_{u_1} + A_{u_2} + A_{u_3}} \quad (2)$$

The results of $[\text{Ce}^{3+}]$ concentration were summarized in Tab.S2. It is pretty straightforward to infer that the concentration of $[\text{Ce}^{3+}]$ in YCC was increased up to 27.90%, which is much higher than that of in CeO_2 (18.13%), Y-doped CeO_2 (22.88%) and CeO_2/PCN (24.17%) samples. It further provides evidence for the existence of strong interaction between CeO_2 and PCN in YCC, benefiting from the stabilization effect for trivalent cerium ions on PCN support [34].

In addition, the O 1s signal can be detected in Fig. 4b. For YCC, the O1s peaks of YCC at 529.49 eV and 532.04 eV were assigned to the lattice oxygen (O_{lat}) and surface oxygen (O_{sur}) of CeO_2 , respectively. The binding energies of lattice oxygen and surface oxygen in YCC both obviously shifted to higher binding energies compared with CeO_2 sample without yttrium doping and PCN hybridization. After deconvolution and multiple-peak separation, we could obtain the concentration of surface oxygen $[\text{O}_{\text{sur}}]$ according to the Eq. (3):

$$[\text{O}_{\text{sur}}] = \frac{A_{\text{O}_{\text{sur}}}}{A_{\text{O}_{\text{sur}}} + A_{\text{O}_{\text{lat}}}} \quad (3)$$

Results for surface active oxygen $[\text{O}_{\text{sur}}]$ were also summarized in Tab.S2. The percentage of $[\text{O}_{\text{sur}}]$ for YCC is approximately 37.16% and this value is much higher than that of other samples. The strong interaction induced by YCC mainly affects the surface oxygen binding energy and it also can enhance the surface oxygen activity [35]. The concentration of oxygen vacancy plays a vital role in regulating the number of photoexcited electron-hole pairs as well as the recombination and separation of them. Thus the photocatalytic performance of YCC with relatively higher concentration of oxygen vacancy may be promoted greatly.

The main features of C 1s were given in Fig. 4c, the characteristic peak at 288.24 eV resulted from the sp^2 -bond carbon($\text{N}=\text{C}=\text{N}$) of PCN, the characteristic peak at 284.69 eV was attributed to the graphitic carbon of PCN [35]. The binding energy of sp^2 -bond carbon in YCC located at 288.14 eV and it decreased about 0.10 eV compared with that of PCN. In Fig. 4d, the N 1s peak of PCN was deconvoluted to three fitted peaks at 398.81 eV , 400.07 eV and 401.3 eV , which would be assigned to the pyridine N, pyrrolic N, and graphitic N, respectively [36]. The binding energy of pyridine N in YCC is 398.65 eV , decreasing 0.16 eV in comparison with PCN. In YCC, the binding energies of C 1s and N 1s peaks were slightly lower than that of PCN, while the binding energies of Ce 3d and O 1s in YCC shifted to higher value than that of CeO_2 counterpart. The oppositely shifting convincingly confirmed the chemical interactions between PCN and Y-doped CeO_2 [37,38]. Therefore, the XPS results fully illustrated the formation of heterojunction in YCC nanocomposite, which was also well consistent with above-mentioned TEM, XRD, FT-IR and Raman analysis results.

3.3. Photocatalytic redox activity

Degradation of RhB pollutant was employed to evaluate the photooxidation activity of samples. As presented in Fig. 5a, the degradation curve of YCC reached 97.12% after 360 min. under visible light irradiation, which is obvious superior to other samples. However CeO_2 and Y-doped CeO_2 samples afforded inferior performance in RhB degradation, attributing to their weak absorption for visible light and small specific surface area. Besides, the kinetic behavior of photocatalytic degradation of RhB was also studied in Fig. 5b. The change of RhB concentration over time follows the first-order kinetics equation according to Eq. (4):

$$-\ln(C/C_0) = kt \quad (4)$$

Where C_0 is the initial concentration of RhB and C is the

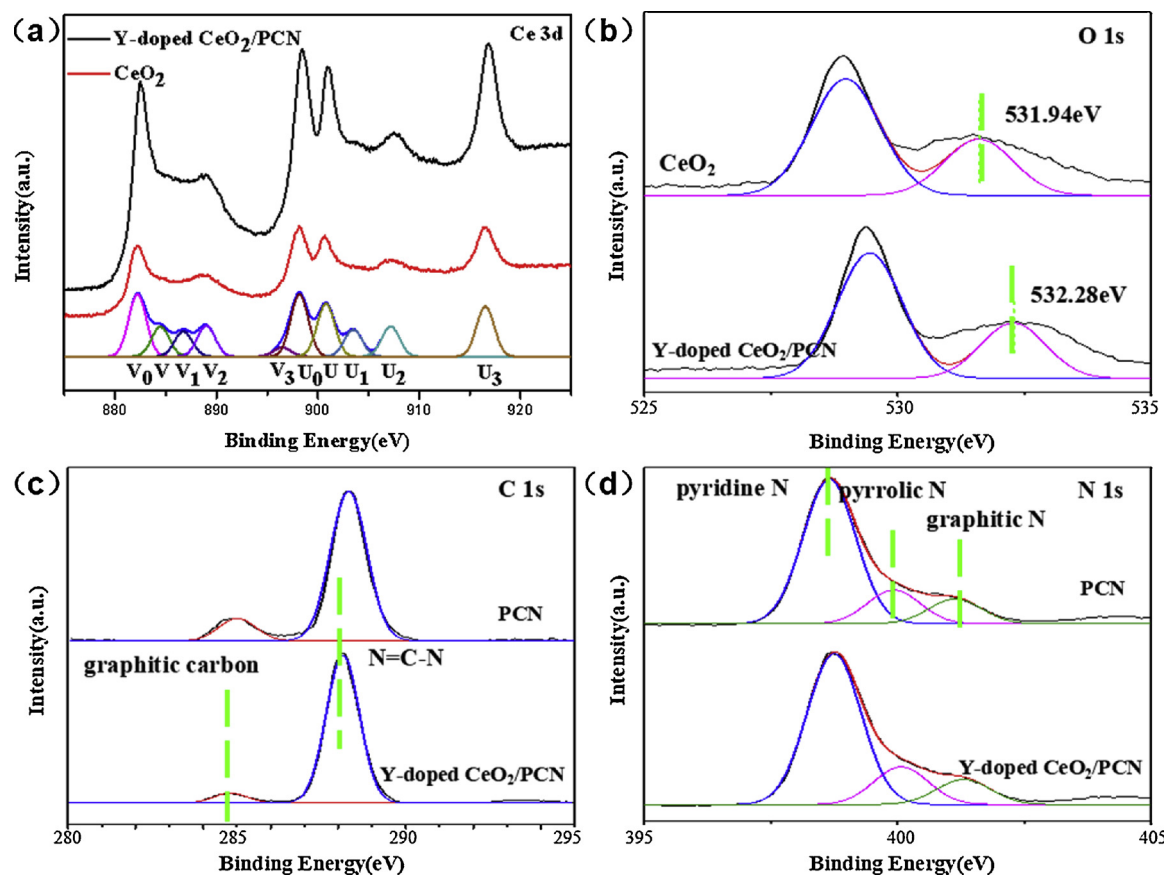


Fig. 4. High resolution of XPS spectra: (a) Ce3d (b) O1s (c) C1s and (d) N1s.

concentration at a particular time. By numerical calculation, the rate constant is consistent with the change in concentration, which indicates that RhB oxidation action follows the law of Langmuir–Hinshelwood rate. Results for rate constant are summarized in the Tab. S3. It is worth noticing that YCC sample achieved 5.97, 4.04 and 1.33 times faster than that of CeO_2 , PCN and CeO_2/PCN in photooxidation removal of RhB containments. In order to study the stability and reproducibility of the photooxidation activity of YCC, another four cycles of photocatalytic degradation RhB tests were further carried out. The results were given in Fig. 5c, illustrating that there is almost no change in the photodegradation rate after five rounds of photocatalytic oxidation processes. Thus the as-fabricated YCC nanocomposited photocatalyst has excellent photocatalytic stability and reusability.

To further evaluate the photoinduced reduction activity of the as-prepared photocatalysts, Fig. 5d shows after 120 min. of visible light radiation, the H_2 production rate of YCC is $48.5 \mu\text{mol h}^{-1}$, which displays 3.74 times and 3.06 times higher than that of CeO_2 ($13.0 \mu\text{mol h}^{-1}$) and PCN ($15.8 \mu\text{mol h}^{-1}$) counterparts, respectively. In addition, the rate of H_2 generation is 24.4 and $28.6 \mu\text{mol h}^{-1}$ for Y-doped CeO_2 and CeO_2/PCN respectively and they are both much lower than that of YCC. In addition, YCC exhibited obviously more adsorption as well as accelerated photocatalytic reduction of Cr(VI) in comparison with pure CeO_2 . (shown in Fig. S8) The degradation rate of YCC reached 98.12% within 4 h, which was 1.61 and 5.79 times higher than pure PCN (60.76%) and CeO_2 (16.94%), respectively. For quantitatively comparing the photocatalytic activities of Cr(VI), the reaction rate constant (k) for each samples was estimated in Tab. S5. YCC reached a highest K value of 0.4287 min^{-1} , which was much higher than pure CeO_2 (0.0127 min^{-1}) and PCN (0.0651 min^{-1}). Therefore, YCC is really a cost-effective bifunctional photocatalyst in view of the simultaneous improvement of the photooxidation activity and photocatalytic reduction capability [39].

3.4. Proposed mechanism

The photocurrent-time response was employed to evaluate the interfacial charge separation dynamics. From the photocurrent response curves given in Fig. 6a, it can be clearly observed that the photocurrent curves of all samples abruptly increase and decrease when switching the light source on and off, indicating their semiconductor intrinsic nature. The photocurrent density of YCC reached $1.41 \mu\text{A}/\text{cm}^2$ and the value is 1.85, 2.71, 1.52 and 1.13 times higher than the value of PCN ($0.76 \mu\text{A}/\text{cm}^2$), CeO_2 ($0.52 \mu\text{A}/\text{cm}^2$), Y-doped CeO_2 ($0.92 \mu\text{A}/\text{cm}^2$) and CeO_2/PCN ($1.24 \mu\text{A}/\text{cm}^2$) respectively. The increased photocurrent reveals that the photogenerated charge carriers in the YCC are separated much more efficiently than that of counterpart samples. Typically, the stronger intensity of photocurrent means the higher transfer efficiency of photogenerated electrons and holes [40,41]. Thus, YCC will generate much more separated photo-induced electrons and holes to participate in the following photocatalytic redox reactions, achieving the better photocatalytic performance. The electrochemical impedance spectra (EIS) Nyquist plots of the pure PCN, CeO_2 , Y-doped CeO_2 , CeO_2/PCN and YCC were shown in Fig. 6b. The semicircle on the EIS plot indicates occurrence of charge transfer. The arc radius of the YCC appears to be much smaller compared with that of PCN and CeO_2 counterparts, confirming that YCC heterojunction can greatly improve the transfer efficiency of photoexcited electron-hole pairs driven by the internal electric field and interfacial interaction [42]. In general, the smaller diameter of the semicircle of the impedance ring means the smaller resistance of photocatalyst electron transport. Moreover it means the separation of photogenerated electrons and holes are faster, which finally affords a better photocatalytic activity [15].

In order to determine the electron hole recombination rate of all samples, the photoluminescence (PL) analysis was conducted and the corresponding PL emission spectrum is shown in Fig. 6c. The pure CeO_2

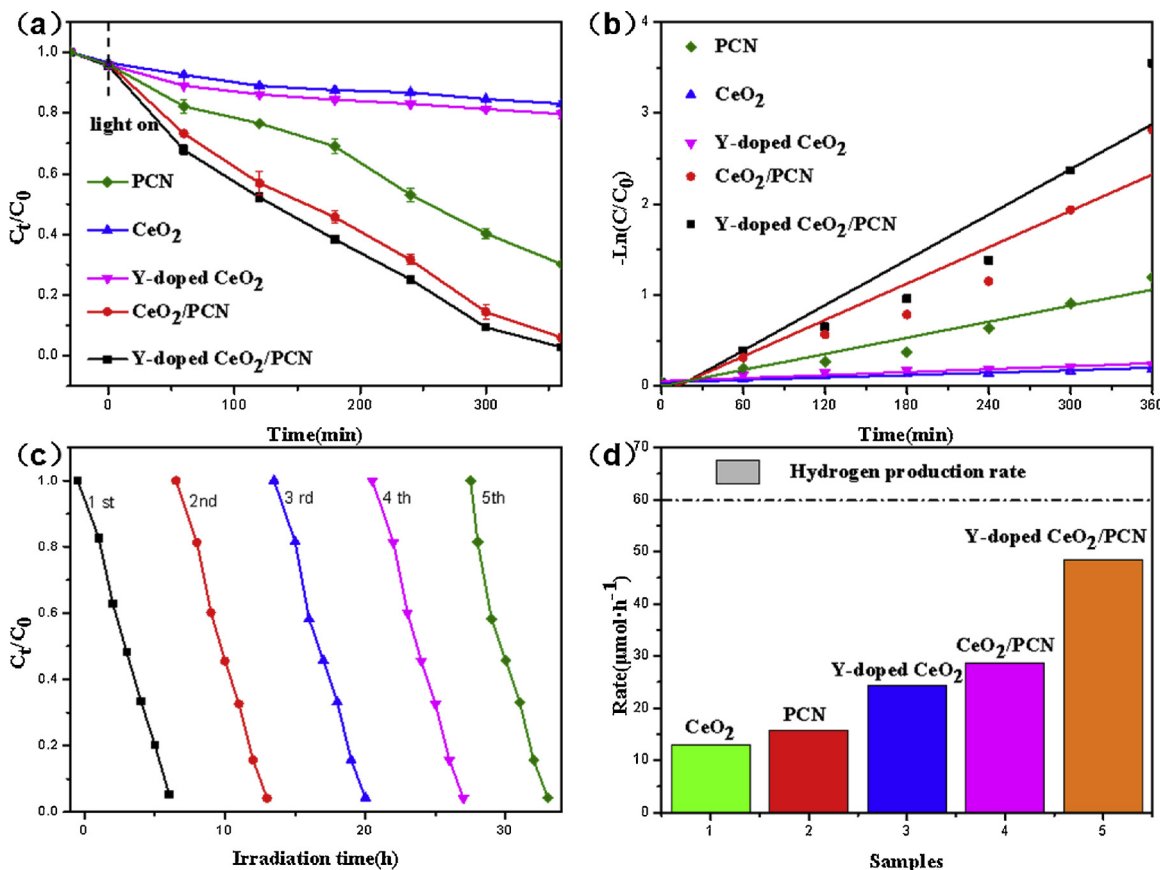


Fig. 5. Photooxidation activity evaluation of as-prepared samples: (a) RhB variation curves; (b) Degradation kinetics; (c) Stability test and (d) Photoreduction activity for H_2 production of samples.

and Y-doped CeO_2 show a strong peak centered at 450 nm attributed to surface defects, which typically exists between the O_{2p} valence band and the Ce_{4f} conduction band [43]. It is well-known that the dominant surface defects in CeO_2 are oxygen vacancies. Intriguingly, the PL emission intensity of CeO_2 and PCN after compositing was both reduced obviously. Therefore, PL studies have shown that coupling PCN with CeO_2 is really a cost-effective approach to reduce the recombination rate of hole and electron pairs for a single component [44]. In particular, YCC sample presents the lowest PL intensity, indicating that it has significantly ameliorated the separation of photo-induced carriers thanks to the well-established heterojunction structure. Subsequently, the photocatalytic redox performance can be promoted distinctly.

In order to definitely probe the promotion mechanism, trapping experiments were used to determine the major active species in the photocatalytic processes. Fig. 6d indicated that the degradation efficiency of RhB was slightly impeded after adding tert-butanol (TBA, 1 mM) as a $\cdot\text{OH}$ scavenger. In addition, $\text{K}_2\text{Cr}_2\text{O}_7$ (1 mM) as electron (e^-) scavenger showed less effect of degradation efficiency. However, when the hole (h^+) scavenger of ethylenediaminetetraacetic acid disodium (EDTA-2Na, 1 mM) was introduced, the degradation efficiency of RhB was significantly reduced. Furthermore, 1, 4-benzoquinone (BQ, 1 mM) as a scavenger of $\cdot\text{O}_2^-$ also showed a large influence on the final degradation rate [45,46]. The results of the active substance capture experiments showed that $\cdot\text{O}_2^-$ and h^+ were the main active substances, while $\cdot\text{OH}$ and e^- had little effect on the degradation of RhB under visible light irradiation. The reactive oxygen species (ROS) $\cdot\text{O}_2^-$ was successfully detected by EPR. As shown in Fig. S9, after 5 min visible light irradiation, the signal of $\cdot\text{OH}$ is very weak and strong $\cdot\text{O}_2^-$ signal peaks are captured in YCC. The result is consistent with the result of the active species trapping experiment.

Based on the above analysis, the schematic diagram of possible

photocatalytic mechanism for YCC was proposed in Fig. 7. Due to the matchable overlapping band energy levels of PCN ($\text{CB} = -1.05 \text{ eV}$, $\text{VB} = 1.57 \text{ eV}$) and CeO_2 ($\text{CB} = -0.87 \text{ eV}$, $\text{VB} = 2.01 \text{ eV}$) deduced from VB-XPS in Fig. S6 and Tauc plot in Fig. 7, they can form an effective charge-separation-type heterojunction structure. Under visible light irradiation, the electrons and holes in YCC are excited and separated, and then the electrons in conduction band (CB) of PCN transfer smoothly to CB of CeO_2 , meanwhile the holes in valence band (VB) of CeO_2 migrate to VB of PCN, establishing a robust built-in electric field in YCC heterojunction interfaces. The built-in electric field well inhibit the recombination of active photo-generated electrons and holes effectively. Finally, as illustrated in Fig. 7a and b, the YCC heterojunction affords expectable photoredox performance for corresponding photooxidation of RhB dye and proton photoreduction to produce hydrogen, because much more photogenerated holes and electrons accumulate accordingly in the CB of CeO_2 and VB of PCN in YCC.

4. Conclusions

In summary, Y-doped CeO_2/PCN hybridized photocatalyst was prepared by a simple in-situ hydrothermal method. The morphology and structure of the as-prepared YCC photocatalyst were thoroughly dissected by various spectroscopic technologies. The bandgap value of the as-prepared YCC nanocomposited photocatalyst was 0.22 eV lower than that of pure CeO_2 . YCC exhibited excellent photoredox performance under visible light irradiation, affording to 5.73- and 3.74-fold higher for RhB degradation and proton photoreduction to produce H_2 than that of pure CeO_2 , respectively. The proposed mechanism illustrated that the matchable band energy alignment of PCN and CeO_2 contributed to a superexcellent YCC heterojunction, promoting the establishment of built-in electric field and separation of photogenerated

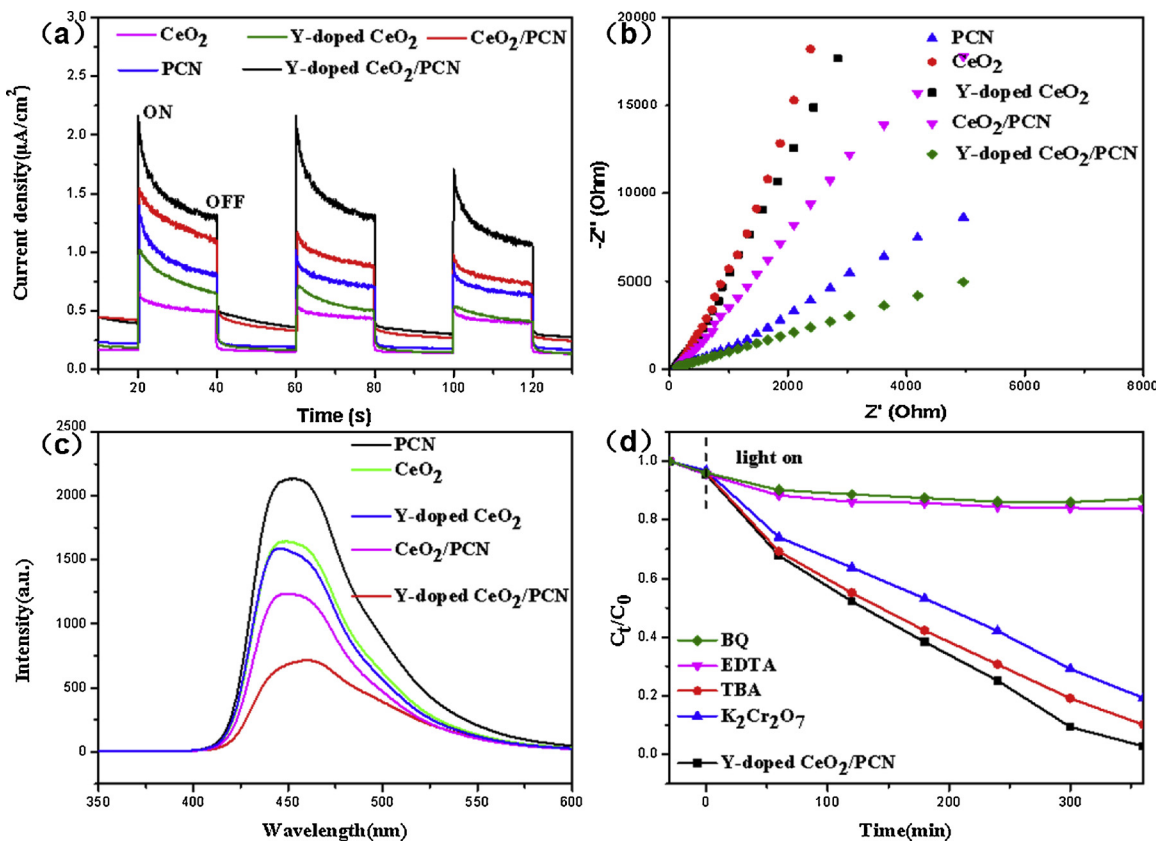


Fig. 6. Photoelectrochemical characterization of as-prepared samples: (a) Transient photocurrent response; (b) EIS Nyquist plots; (c) PL spectra and (d) Degradation of RhB with the addition of BQ, EDTA, TBA and $K_2Cr_2O_7$.

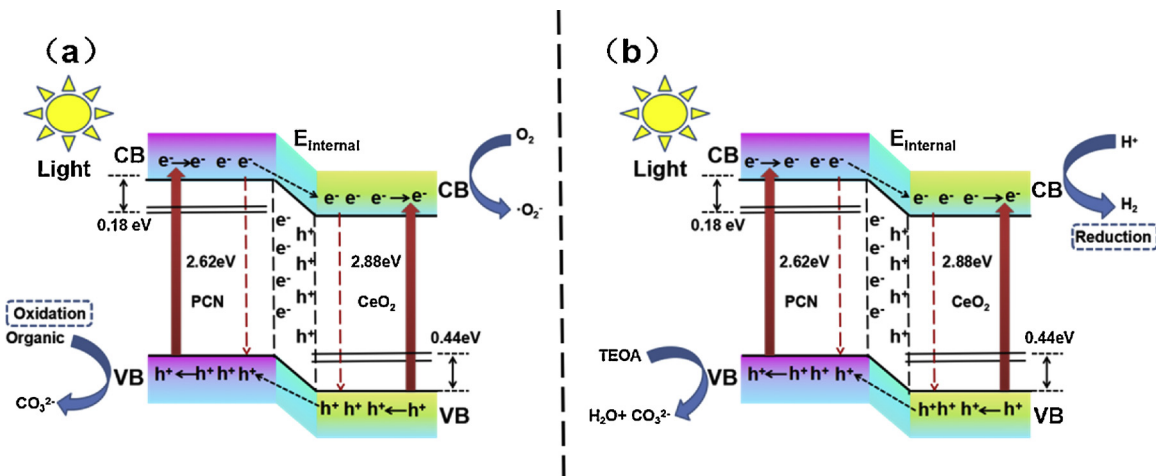


Fig. 7. Proposed mechanism for photoredox promotion by YCC photocatalyst.

holes and electrons to afford the final superior photoredox performance. Consequently, this study can provide a cost-effective route to drive the photogenerated electrons and holes in photocatalyst to involve various redox reactions.

Acknowledgements

This work was financially supported by the National Natural Science Foundation of China (No. 21805191 and 21307104), the Major Projects of Nature Science Research in Universities and Colleges in Jiangsu Province, China (No. 16KJA150008), Shenzhen Peacock Plan (No. 20180921254c) and the JST ACT-C program of Japan.

Appendix A. Supplementary data

Supplementary material related to this article can be found, in the online version, at doi: <https://doi.org/10.1016/j.apcatb.2018.10.057>.

References

- [1] D.-m. Chen, G. Xu, L. Miao, S. Nakao, P. Jin, Sputter deposition and computational study of $M-TiO_2$ ($M = Nb, Ta$) transparent conducting oxide films, *Surf. Coat. Technol.* 206 (2011) 1020–1023.
- [2] T. Fu, J.-m. Sun, Z. Alajmi, F. Wu, Sol-gel preparation, corrosion resistance and hydrophilicity of Ta-containing TiO_2 films on Ti_6Al_4V alloy, *Trans. Nonferrous Met. Soc. China* 25 (2015) 471–476.
- [3] J.W. Pan, C. Li, Y.F. Zhao, R.X. Liu, Y.Y. Gong, L.Y. Niu, X.J. Liu, B.Q. Chi,

Electronic properties of TiO_2 doped with Sc, Y, La, Zr, Hf, V, Nb and Ta, *Chem. Phys. Lett.* 628 (2015) 43–48.

[4] A. Bueno-López, Diesel soot combustion ceria catalysts, *Appl. Catal. B Environ.* 146 (2014) 1–11.

[5] C.-i. Lee, Q.-l. Meng, H. Kaneko, Y. Tamaura, Dopant effect on hydrogen generation in two-step water splitting with $\text{CeO}_2\text{-ZrO}_2\text{-MO}_x$ reactive ceramics, *Int. J. Hydrogen Energy* 38 (2013) 15934–15939.

[6] G. Qi, R.T. Yang, Performance and kinetics study for low-temperature SCR of NO with NH_3 over $\text{MnO}_x\text{-CeO}_2$ catalyst, *J. Catal.* 217 (2003) 434–441.

[7] A. Trovarelli, Catalytic properties of ceria and CeO_2 -containing materials, *Catal. Rev.* 38 (1996) 439–520.

[8] D. Jampaiah, K.M. Tur, P. Venkataswamy, S.J. Ippolito, Y.M. Sabri, J. Tardio, S.K. Bhargava, B.M. Reddy, Catalytic oxidation and adsorption of elemental mercury over nanostructured $\text{CeO}_2\text{-MnO}_x$ catalyst, *RSC Adv.* 5 (2015) 30331–30341.

[9] W. Shan, F. Liu, Y. Yu, H. He, The use of ceria for the selective catalytic reduction of NO_x with NH_3 , *Chin. J. Catal.* 35 (2014) 1251–1259.

[10] B. Mandal, A. Mondal, Solar light sensitive samarium-doped ceria photocatalysts: microwave synthesis, characterization and photodegradation of Acid Orange 7 at atmospheric conditions and in the absence of any oxidizing agents, *RSC Adv.* 5 (2015) 43081–43091.

[11] J. Saranya, K.S. Ranjith, P. Saravanan, D. Mangalaraj, R.T. Rajendra Kumar, Cobalt-doped cerium oxide nanoparticles: enhanced photocatalytic activity under UV and visible light irradiation, *Mater. Sci. Semicond. Process.* 26 (2014) 218–224.

[12] I. Florea, C. Feral-Martin, J. Majimel, D. Ihiawakrim, C. Hirlimann, O. Ersen, Three-dimensional tomographic analyses of CeO_2 nanoparticles, *Cryst. Growth Des.* 13 (2013) 1110–1121.

[13] J.P.Y. Tan, H.R. Tan, C. Boothroyd, Y.L. Foo, C.B. He, M. Lin, Three-dimensional structure of CeO_2 nanocrystals, *J. Phys. Chem. C* 115 (2011) 3544–3551.

[14] M.J. Bojdys, J.O. Muller, M. Antonietti, A. Thomas, Ionothermal synthesis of crystalline, condensed, graphitic carbon nitride, *Chemistry* 14 (2008) 8177–8182.

[15] N. Tian, H. Huang, C. Liu, F. Dong, T. Zhang, X. Du, S. Yu, Y. Zhang, In situ copyrolysis fabrication of $\text{CeO}_2\text{/g-C}_3\text{N}_4$ n–n type heterojunction for synchronously promoting photo-induced oxidation and reduction properties, *J. Mater. Chem. A* 3 (2015) 17120–17129.

[16] X. Wang, S. Blechert, M. Antonietti, Polymeric graphitic carbon nitride for heterogeneous photocatalysis, *ACS Catal.* 2 (2012) 1596–1606.

[17] Q. Zhang, B. Xu, S. Yuan, M. Zhang, T. Ohno, Improving g-C₃N₄ photocatalytic performance by hybridizing with $\text{Bi}_2\text{O}_2\text{CO}_3$ nanosheets, *Catal. Today* 284 (2017) 27–36.

[18] Q. Zhang, S. Yuan, B. Xu, Y. Xu, K. Cao, Z. Jin, C. Qiu, M. Zhang, C. Su, T. Ohno, A facile approach to build $\text{Bi}_2\text{O}_2\text{CO}_3\text{/PCN}$ nanohybrid photocatalysts for gaseous acetaldehyde efficient removal, *Catal. Today* 315 (2018) 184–193.

[19] Z. Zhao, Y. Sun, F. Dong, Graphitic carbon nitride based nanocomposites: a review, *Nanoscale* 7 (2015) 15–37.

[20] L. Wu, S. Fang, L. Ge, C. Han, P. Qiu, Y. Xin, Facile synthesis of Ag@CeO_2 core-shell plasmonic photocatalysts with enhanced visible-light photocatalytic performance, *J. Hazard. Mater.* 300 (2015) 93–103.

[21] X. Zhang, X. Xie, H. Wang, J. Zhang, B. Pan, Y. Xie, Enhanced photoresponsive ultrathin graphitic-phase C₃N₄ nanosheets for bioimaging, *J. Am. Chem. Soc.* 135 (2013) 18–21.

[22] B. Xu, Q. Zhang, S. Yuan, M. Zhang, T. Ohno, Morphology control and characterization of broom-like porous CeO_2 , *Chem. Eng. J.* 260 (2015) 126–132.

[23] X. Zhang, X. Xie, H. Wang, J. Zhang, B. Pan, Y. Xie, Enhanced photoresponsive ultrathin graphitic-phase C₃N₄ nanosheets for bioimaging, *J. Am. Chem. Soc.* 135 (2013) 18–21.

[24] A. Rangaswamy, P. Sudarsanam, B.G. Rao, B.M. Reddy, Novel molybdenum–cerium based heterogeneous catalysts for efficient oxidative coupling of benzylamines under eco-friendly conditions, *Res. Chem. Intermed.* 42 (2015) 4937–4950.

[25] J. Ciston, R. Si, J.A. Rodriguez, J.C. Hanson, A. Martínez-Arias, M. Fernández-García, Y. Zhu, Morphological and structural changes during the reduction and reoxidation of CuO/CeO_2 and $\text{Ce}_1\text{-xCu}_x\text{O}_2$ nanocatalysts: in situ studies with environmental TEM, XRD, and XAS, *J. Phys. Chem. C* 115 (2011) 13851–13859.

[26] F. Zhang, S.-W. Chan, J.E. Spanier, E. Apak, Q. Jin, R.D. Robinson, I.P. Herman, Cerium oxide nanoparticles: size-selective formation and structure analysis, *Appl. Phys. Lett.* 80 (2002) 127–129.

[27] X.D. Zhou, W. Huebner, Size-induced lattice relaxation in CeO_2 nanoparticles, *Appl. Phys. Lett.* 79 (2001) 3512–3514.

[28] J. Zhang, X. Chen, K. Takanabe, K. Maeda, K. Domen, J.D. Epping, X. Fu, M. Antonietti, X. Wang, Synthesis of a carbon nitride structure for visible-light catalysis by copolymerization, *Angew. Chem. Int. Ed. Engl.* 49 (2010) 441–444.

[29] J. Liu, T. Zhang, Z. Wang, G. Dawson, W. Chen, Simple pyrolysis of urea into graphitic carbon nitride with recyclable adsorption and photocatalytic activity, *J. Mater. Chem.* 21 (2011) 14398.

[30] Z. Abbasi, M. Haghighi, E. Fatehifar, N. Rahemi, Comparative synthesis and physicochemical characterization of CeO_2 nanopowder via redox reaction, precipitation and sol-gel methods used for total oxidation of toluene, *Asia-Pac. J. Chem. Eng.* 7 (2012) 868–876.

[31] X. Zhang, X. Xie, H. Wang, J. Zhang, B. Pan, Y. Xie, Enhanced photoresponsive ultrathin graphitic-phase C₃N₄ nanosheets for bioimaging, *J. Am. Chem. Soc.* 135 (2013) 18–21.

[32] S. Hu, F. Zhou, L. Wang, J. Zhang, Preparation of $\text{Cu}_2\text{O/CeO}_2$ heterojunction photocatalyst for the degradation of Acid Orange 7 under visible light irradiation, *Catal. Commun.* 12 (2011) 794–797.

[33] X. Yao, C. Tang, Z. Ji, Y. Dai, Y. Cao, F. Gao, L. Dong, Y. Chen, Investigation of the physicochemical properties and catalytic activities of $\text{Ce}_{0.67}\text{M}_{0.33}\text{O}_2$ ($\text{M} = \text{Zr}^{4+}$, Ti^{4+} , Sn^{4+}) solid solutions for NO removal by CO, *Catal. Sci. Technol.* 3 (2013) 688–698.

[34] S. Hu, F. Zhou, L. Wang, J. Zhang, Preparation of $\text{Cu}_2\text{O/CeO}_2$ heterojunction photocatalyst for the degradation of Acid Orange 7 under visible light irradiation, *Catal. Commun.* 12 (2011) 794–797.

[35] Y. He, Y. Wang, L. Zhang, B. Teng, M. Fan, High-efficiency conversion of CO_2 to fuel over $\text{ZnO/g-C}_3\text{N}_4$ photocatalyst, *Appl. Catal. B Environ.* 168–169 (2015) 1–8.

[36] H. Ji, F. Chang, X. Hu, W. Qin, J. Shen, Photocatalytic degradation of 2,4,6-trichlorophenol over g-C₃N₄ under visible light irradiation, *Chem. Eng. J.* 218 (2013) 183–190.

[37] S.-W. Cao, Y.-P. Yuan, J. Barber, S.C.J. Loo, C. Xue, Noble-metal-free g-C₃N₄/Ni (dmgh)₂ composite for efficient photocatalytic hydrogen evolution under visible light irradiation, *Appl. Surf. Sci.* 319 (2014) 344–349.

[38] Z. Huang, Q. Sun, K. Lv, Z. Zhang, M. Li, B. Li, Effect of contact interface between TiO_2 and g-C₃N₄ on the photoreactivity of g-C₃N₄/TiO₂ photocatalyst: (001) vs (101) facets of TiO_2 , *Appl. Catal. B Environ.* 164 (2015) 420–427.

[39] L. Huang, Y. Li, H. Xu, Y. Xu, J. Xia, K. Wang, H. Li, X. Cheng, Synthesis and characterization of $\text{CeO}_2\text{/g-C}_3\text{N}_4$ composites with enhanced visible-light photocatalytic activity, *RSC Adv.* 3 (2013) 22269.

[40] B. Xu, Q. Zhang, S. Yuan, M. Zhang, T. Ohno, Synthesis and photocatalytic performance of yttrium-doped CeO_2 with a porous broom-like hierarchical structure, *Appl. Catal. B Environ.* 183 (2016) 361–370.

[41] P. Dumrongrojathanath, T. Thongtem, A. Phuruangrat, S. Thongtem, Hydrothermal synthesis of Bi_2WO_6 hierarchical flowers with their photonic and photocatalytic properties, *Superlattices Microstruct.* 54 (2013) 71–77.

[42] F. Deng, Y. Liu, X. Luo, D. Chen, S. Wu, S. Luo, Enhanced photocatalytic activity of $\text{Bi}_2\text{WO}_6\text{/TiO}_2$ nanotube array composite under visible light irradiation, *Sep. Purif. Technol.* 120 (2013) 156–161.

[43] G. Wang, Q. Mu, T. Chen, Y. Wang, Synthesis, characterization and photoluminescence of CeO_2 nanoparticles by a facile method at room temperature, *J. Alloys Compd.* 493 (2010) 202–207.

[44] D. Channei, B. Inceesungvorn, N. Wetchakun, S. Ukitnukun, A. Nattestad, J. Chen, S. Phanichphant, Photocatalytic degradation of methyl orange by CeO_2 and Fe-doped CeO_2 films under visible light irradiation, *Sci. Rep.* 4 (2014) 5757.

[45] N. Tian, H. Huang, C. Liu, F. Dong, T. Zhang, X. Du, S. Yu, Y. Zhang, In situ copyrolysis fabrication of $\text{CeO}_2\text{/g-C}_3\text{N}_4$ n–n type heterojunction for synchronously promoting photo-induced oxidation and reduction properties, *J. Mater. Chem. A* 3 (2015) 17120–17129.

[46] P. Ji, J. Zhang, F. Chen, M. Anpo, Study of adsorption and degradation of acid orange 7 on the surface of CeO_2 under visible light irradiation, *Appl. Catal. B Environ.* 85 (2009) 148–154.